Validation and Application of the Axisymmetric Analogue Technique on Rapid Hypersonic Shape Optimisation

Brchnelová, M.; Mooij, E.

DOI
10.2514/6.2022-0146

Publication date
2022

Document Version
Final published version

Published in
AIAA SCITECH 2022 Forum

AIAA SciTech Forum
January 3-7, 2022, San Diego, CA & Virtual
AIAA SCITECH 2022 Forum

10.2514/6.2022-0146

Validation and Application of the Axisymmetric Analogue Technique on Rapid Hypersonic Shape Optimisation

Michaela Brchnelova*
Catholic University Leuven, Faculty of Science, Department of Mathematics
Celestijnenlaan 200B, 3000 Leuven, Belgium

Erwin Mooij†
Delft University of Technology, Faculty of Aerospace Engineering,
Kluyverweg 1, 2629 HS Delft, The Netherlands

The beginning of the conceptual design phase of (re)entry missions requires aerodynamic methods to reduce the initial design space. For this purpose, full computational fluid dynamics (CFD) simulations are unsuitable due to their computational requirements. Rapid hypersonic methods are thus often employed to approximate the heat flux and skin friction on the most critical parts of the (re)entry vehicle, such as the nose and the leading edges. However, the vast majority of these rapid methods only allow for a computation of these parameters at specific fixed locations and not on the other parts of the vehicle. One method that overcomes this is the axisymmetric analogue method, that determines the entire viscous flowfield from the inviscid flowfield solution. This method has typically been coupled to inviscid Euler simulations, but even Euler simulations can still consume a lot of computational time. In earlier research, it was shown that a reasonable accuracy can also be obtained if this method is coupled with the inviscid flowfield computed via the modified Newtonian technique. In this paper, we extend the validation and estimation of the uncertainties of this method using CFD, evaluate the respective corrections for thermal and chemical fluxes separately, and apply these corrections back to the solver. The biconic DART vehicle, partial optimisation of which was presented in the previous paper, is revisited, here optimising only four parameters instead of five as originally intended, as using five parameters resulted in an unfeasible geometry. We perform a full response surface methodology and analysis of variance accounting for the CFD corrections and examine the final optimised design also again with the Newtonian/axisymmetric code. The proposed methodology leads to a small underestimate of the heat fluxes, but is considered sufficient for the conceptual design phase.

I. Introduction

Full 3D computational fluid dynamics (CFD) solutions are very expensive for hypersonic flows, especially when aspects such as chemistry and radiation are taken into account. In particular, during the initial design phases while exploring the design space, the accuracy of a full CFD solution is often not required. For this reason, a rapid hypersonic method has been developed in previous work,[1] based on the technique of the axisymmetric analogue that determines the viscous parameters from a pre-computed inviscid flowfield, originally suggested by Cooke.[2] In the past, this method has been extensively used on Space Shuttle configurations and showed a good agreement with experimental data.[3–6] In the previous work, this viscous technique has been coupled with the inviscid flowfield computed with the modified Newtonian method.

*PhD candidate, m.brchnelova@gmail.com, Student Member AIAA.
†Associate Professor, section Astrodynamics and Space Missions, e.mooij@tudelft.nl, Associate Fellow AIAA.

Firstly, in the previous paper, this method has been applied to various Space Shuttle cases at different freestream conditions and with varying scales, as means of initial validation. It was also noted that several aspects were still missing in this technique, such as the estimation of the uncertainty for not accounting for the geometrical effects of the biconic design (which cannot be well captured by the modified Newtonian technique), the additional heat fluxes due to chemistry and radiation, and better evaluation of the leeward pressure coefficient, as this is important for the centre of pressure calculation. These effects can be studied through comparisons with the CFD data, since CFD allows one to separate these effects from one another (for example, the thermal, radiative and chemical fluxes). First, an additional validation of the current Newtonian/axisymmetric analogue technique is performed with the FIRE-II test case, which is considered the standard for validating hypersonic solvers and determining their uncertainty against published CFD results.[7] Afterwards, a CFD model is developed based on the COOLFluiD (Computational Object-Oriented Libraries for Fluid Dynamics) platform,[8] which will be, for these flight conditions, also validated against the FIRE-II data from other CFD studies. This CFD model will then be used to simulate the configurations at hand for optimisation at the points of their peak aerodynamic heating, which are the most crucial for the design, and compared to the current method's predictions. This way, two aspects can be investigated; i) the accuracy of the evaluation of the thermal fluxes, which the current method aims to focus on and ii), the peak contribution of the chemical fluxes, which are not computed by the current method but which still have to be estimated to create reliable data for shape optimisation, as their magnitude depends on the geometry. For now, the effects of the radiative fluxes are neglected, as they are typically not so important for Earth entry, at least when the uncertainties of the applied method are taken into account.

Secondly, in the previous paper, this method was used for a limited optimisation study of the biconic DART module, originally studied by Sudmeijer and Mooij in 2002.[10] This optimisation was, however, incomplete, since the study mainly focused on the comparison rather than optimisation of the heat fluxes and since one of the configurations was found to be geometrically infeasible it violated the design-space orthogonality of the applied design method. Here, we aim to apply our methodology to corrected shapes and in addition to the comparison of the heat fluxes, also to derive the optimal design based on the response-surface methodology.

The first section of this paper Sec. II, summarises the theory behind the method of the axisymmetric analogue and the response surface design optimisation methodology. Section III evaluates the performance of the developed CFD model and the current Newtonian/axisymmetric method against the FIRE-II experiment. Afterwards, Sec. IV discusses the implementation of an improved computation of the leeward pressure coefficient and its effects. Section V introduces the biconic DART module and the optimisation study parameters. Before the designs are analysed, the results of the Newtonian/axisymmetric method are compared with those of the CFD model: the results of the thermal and overall heat flux comparisons are presented in Sec. VI. Using the found corrections, the setup of the Newtonian/axisymmetric runs is summarised in Sec. VII. Section VIII shows and discusses the optimisation study results. Finally, all the findings are elaborated on and concluded in Sec. IX.

II. Theory

To introduce the methodology, the theory behind the aerodynamic simulation tool developed will be shortly touched upon, with more details to be found in the previous paper.[1] In all the derivations below, the geometry considered is such that the freestream velocity is aligned with the positive x-axis.

A. Inviscid Calculations

For calculation of the inviscid flowfied, the modified Newtonian technique is applied,[11] with the freestream Mach number M_∞ and the ratio of specific heats γ, giving the pressure ratio

$$\frac{p_{O_2}}{p_\infty} = \left[\frac{(\gamma+1)^2 M_\infty^2}{4\gamma M_\infty^2 - 2(\gamma-1)}\right]^{\frac{-\gamma}{\gamma-1}} \left[\frac{1-\gamma+2\gamma M_\infty^2}{\gamma+1}\right] \tag{1}$$

and resulting in the pressure coefficient C_p, for a panel at an angle of θ_i with respect to freestream, of

$$C_{p_i} = C_{p_{max}} \sin^2\theta_i \quad \text{with} \quad C_{p_{max}} = \frac{2}{\gamma M_\infty^2}\left(\frac{p_{O_2}}{p_\infty} - 1\right) \tag{2}$$

The velocity field (in terms of the Mach number) is then determined from the pressure coefficients with the resulting velocity vector assumed to be aligned with the local panel geometry. Then, from the normal and oblique shock relations, and from the velocity and pressure field, the temperature and density are determined. These are then considered to be the boundary-layer-edge values for viscous calculations.

B. Viscous Calculations

To compute the properties in the boundary layer, the modified Eckert's reference temperature method is applied as in Ref. 12, defined by a temperature somewhere in the boundary layer T^*. Assuming a Prandtl number Pr giving laminar and turbulent recovery factors $r_{\text{lam.}}$ and $r_{\text{turb.}}$, this is

$$T^* = T_e\left(0.45 + 0.55\frac{T_w}{T_e} + 0.16r\frac{\gamma-1}{2}M_e^2\right) \quad \text{with} \quad r_{\text{lam.}} = \sqrt{Pr}, \quad r_{\text{turb.}} = Pr^{1/3} \tag{3}$$

where the variables with the w subscript refer to the wall parameters and those with e refer to the boundary-layer-edge parameters. The reference viscosity and density are then evaluated from the reference temperature computed above, using Sutherland's formula for viscosity and the ideal gas law for density.

The technique to get the heat-transfer rate and the skin-friction drag with the axisymmetric analogue has been in use since it was first derived by Cooke in 1961.[2] This method is based on the translation of the 2D geometry to 3D, for which the *metric coefficient* h is required, computed in this paper using the method of Parzhikar.[13] The metric coefficient can be understood as a local 3D representation of the radius which would exist at a particular point in axisymmetric space.

The stagnation-point heating is determined according to Ref. 14 as

$$q_{w_s} = 0.767(\rho\mu)_{e,s}^{0.43}(\rho\mu)_{w,s}^{0.07}\left(\frac{\mathrm{d}u}{\mathrm{d}S}\right)_{e,s}^{0.5}(H_s - H_w)(Pr)^{-0.6} \quad \text{with} \quad \left(\frac{\mathrm{d}u}{\mathrm{d}S}\right)_{e,s} \approx \frac{1}{\epsilon}\sqrt{2\frac{p_e - p_\infty}{\rho_w}} \tag{4}$$

where the subscripts e, s are the stagnation-point edge properties whereas w, s the stagnation-point wall properties. To evaluate the boundary-layer momentum-thickness integral in the stagnation region, the following method is used[15]

$$\int_0^s \rho^* u_e \mu^* h^2 \mathrm{d}s = (\rho^*\mu^*)_s u_{e,\epsilon} h_\epsilon^2 \frac{\Delta s}{4} \tag{5}$$

in which the viscosity and density are evaluated at the stagnation point directly.

The heat flux and the skin friction coefficient are then determined through downstream boundary-layer integration starting from the ϵ stagnation region. In laminar flow, the boundary-layer momentum thickness, θ_L, can be approximated as

$$\theta_L = 0.664\frac{\left(\int_0^s \rho^*\mu_e\mu^* h^2 \mathrm{d}s\right)^{0.5}}{\rho_e u_e h} \tag{6}$$

resulting in the heat flux, $\dot{q}_{w,L}$, and skin friction C_f

$$\dot{q}_{w,L} = 0.22\frac{1}{R_{\theta,e}}\frac{\rho^*}{\rho_e}\frac{\mu^*}{\mu_e}\rho_e u_e(H_{aw} - H_w)Pr_w^{-0.6} \quad \text{and} \quad C_f = \frac{2\dot{q}_{w,L}Pr^{2/3}}{\rho_e u_e\left(H_{aw} - H_w\right)} \tag{7}$$

Once the flow turns turbulent, in a form similar to laminar flow, the momentum-boundary-layer thickness, θ_T, can be approximated by[2]

$$\theta_T = \frac{\left(c_2\int_0^s \mu^{*^m}\rho^* U_e h^{c_3}\mathrm{d}s\right)^{c_4}}{\rho_e U_e h} \tag{8}$$

with the following definitions of the turbulent constants c_1 through c_5

$$c_5 = 2.2433 + 0.93N \quad c_3 = 1 + m \quad c_4 = \frac{1}{c_3} \quad c_2 = (1+m)c_1 \quad c_1 = \frac{c_5^{-2N/(N+1)}}{\left[\frac{N}{(N+1)(N+2)}\right]^{-m}} \tag{9}$$

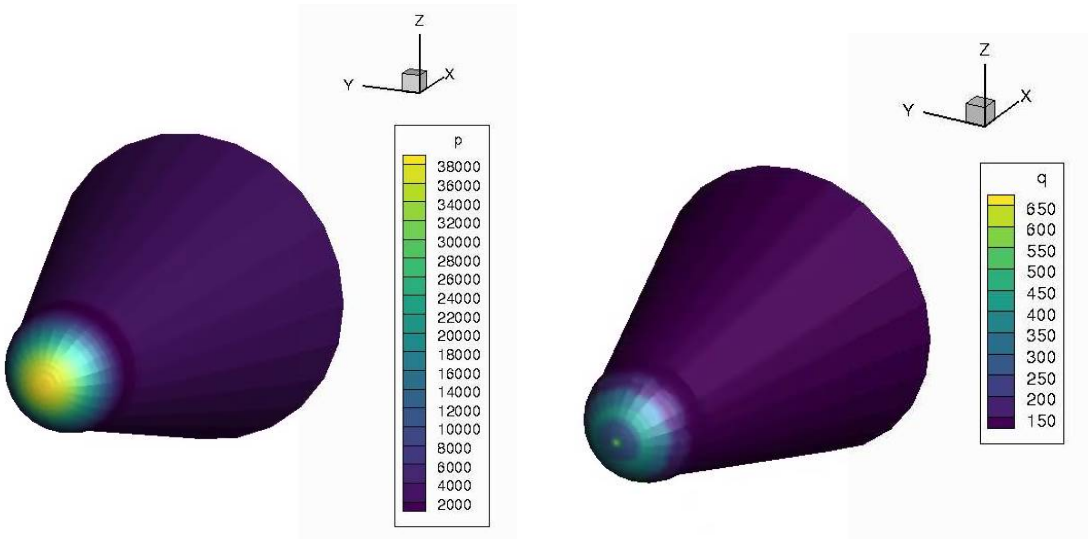

Figure 1. Example pressure and heat-flux distributions as approximated by the Newtonian/axisymmetric analogue method for one of the DART configurations.[1]

The term N can be evaluated as a function of the momentum-thickness-based Reynolds number from the published data,[20] $N = 12.67 - 6.5 \log R_{\theta_e} + 1.21 \log^2 R_{\theta_e}$. This results in $\dot{q}_{w_T}$ and C_f of

$$\dot{q}_{w_T} = c_1 \frac{1}{Re_{\theta_e}^m} \left(\frac{\mu^*}{\mu_e}\right)^m \frac{\rho^*}{\rho_e} \rho_e U_e (H_{aw} - H_w)(Pr)^{-0.4} \quad \text{and} \quad C_f = 2c_1 \left(\frac{1}{Re_{\theta,e}^m}\right) \tag{10}$$

Two different transition criteria are in use (see Ref. 11); $Re_T = 6.421\mathrm{e}^{1.209 \cdot 10^{-4} M_e^{2.641}}$ and $\frac{Re_{\theta_T}}{M_e} = 100$.

These expressions are assessed at each step of each streamline from the ϵ line until the original node location is reached from which the streamline originally emanated. The final values at the end of the streamline are then representative of the heat flux and skin friction at that node. As a result, this code allows for a rough reconstruction of the inviscid and viscous variables, such as the surface heat flux and the momentum boundary-layer thickness on the entire windward side of the vehicle. Example pressure and heat flux distributions, with data taken from the previous study, are shown in Figure 1.

C. Design Optimisation using Surface Response Methodology

For design-space screening and rudimentary optimisation, the so-called response surface methodology (RSM) is used. This method is particularly suitable when an individual design evaluation is costly in terms of CPU load and/or manual labour, and a full-blown numerical optimisation is out of the question. With a cleverly selected number of designs, response surfaces of selected performance criteria can be established that are subsequently used for the optimisation process. The optimum found can, of course, only be a sub-optimum, but the corresponding design may give a good indication of the search direction. The quality of the optimum has to be assessed by an analysis of this design using the original design tools.[21] A further advantage of the method is that when the variation of designs is sufficiently large and covers the design space well, additional insight in the design problem is obtained.

The design method of choice is the so-called central composite design (CCD).[22] Here, a subset of the configurations is based on a (fractional) factorial design that provides the sensitivity to a linear variation of the independent parameters, as well as first-order interactions[a]. Next, per design parameter two extreme points, which are called the axial points, are set, and one or more centre points (*i.e.,* the nominal configuration) are chosen. The latter combination of points will allow for the estimation of quadratic sensitivities in the

[a]An interaction is said to exist when varying one independent parameter at a certain value of a second parameter, will give a different response when the value of the second parameter is changed. Suppose we vary x_1 from 1 to 5 at $x_2 = 2$, which gives the response values of 3 and 4. Suppose we would change x_2 to 3, and the responses would change to 6 and 8, it is said that there is no interaction, because both response values change to the same extent (doubling, in this case). However, suppose that the responses would change to 6 and 0, then an interaction effect is at play.

design, making the response surfaces second-order models. It is noted that the independent variables are commonly normalised, with [-1,+1] spanning the range for the factorial part, and $\pm\alpha$ for the axial points. In the current study, $\alpha = \sqrt{2}$.[22]

The second-order response surface, underlying many engineering problems, is given by

$$\hat{y} = b_0 + \sum_{i=1}^{k} b_i x_i + \sum_{i=1}^{k} b_{ii} x_i^2 + \sum_{i=1}^{k-1} \sum_{j=i+1}^{k} b_{ij} x_i x_j \tag{11}$$

with $\hat{y}$ being the fitted objective, and $b_{..}$ being the coefficients to be estimated, *e.g.,* through the method of least squares. In case of N observations of a response, y_i, its mean, $\bar{y}$, is given by $\bar{y} = \frac{1}{N} \sum_{j=1}^{N} y_j$. The sum of the squared deviation from this mean (or the total variation in the set of observations) is represented by the *total sum of squares*, S_T.

$$S_T = \sum_{i=1}^{N} (y_i - \bar{y})^2 \tag{12}$$

In case the response data is fitted by a response surface – and the independent variables are normalised around zero – the mean value is represented by b_0, see Eq. (11). The relative values of the other coefficients give the sensitivity of this mean response to a variation in the individual factors and interactions. Of course it should be clear that the computed response surface has to fit the responses well. The *residual* r_i is the difference between the measured and predicted response, *i.e.,* $r_i = y_i - \hat{y}_i$. The *predicted response* $\hat{y}_i, i = 1, \cdots, N$, is the response value computed with the response surface using the same factor combination that resulted in the measured value. Three sums of squares can thus be defined, the total sum of squares (S_T), given by Eq. (12), as well as the sum of squares due to regression, S_R, and the sum of squares unaccounted for by the response surface, S_E:

$$S_R = \sum_{i=1}^{N} (\hat{y}_i - \bar{y})^2, \qquad S_E = \sum_{i=1}^{N} (y_i - \hat{y}_i)^2 \tag{13}$$

A first indication of the goodness of fit is given by the *coefficient of determination*, R^2, defined by the ratio of the sum of squares of the residual and the total sum of squares:

$$R^2 = \frac{S_R}{S_T} \tag{14}$$

A better statistic, however, is the adjusted coefficient of determination that takes the degrees of freedom, p, taken up by all the terms included in Eq. (11) into account:

$$R_A^2 = 1 - (1 - R^2) \frac{N - 1}{N - p} \tag{15}$$

More details on the application of response-surface methodology can be found in the quoted references.

III. Fire-II Validation of the Current Method and the CFD Model

A solver based on the Newtonian method only to estimate the inviscid field is going to be frequently inaccurate, especially in conditions in which the modified Newtonian method does not provide a good pressure-coefficient estimate (zones of complex geometry or corner/ leeward regions). In addition, this technique can only predict convective heat flux and no other (*e.g.,* chemistry or radiation).

In earlier work, the results of the solver were compared for a cone and a few Space Shuttle configurations at different flight conditions and scales. Comparisons were mostly made to the validated data also computed using the axisymmetric analogue, but with the Euler inviscid flowfield instead of the modified Newtonian method. The most basic tests, which are typically performed while validating hypersonic software, such as the FIRE-II test flight, were not yet performed. From these very simple and well known configurations, it could be determined with higher certainty what accuracy can be expected from the solver at different conditions and specifically at conditions at which chemistry and radiation are also important. Thus, this test case was also performed before the solver was applied to the DART configurations.

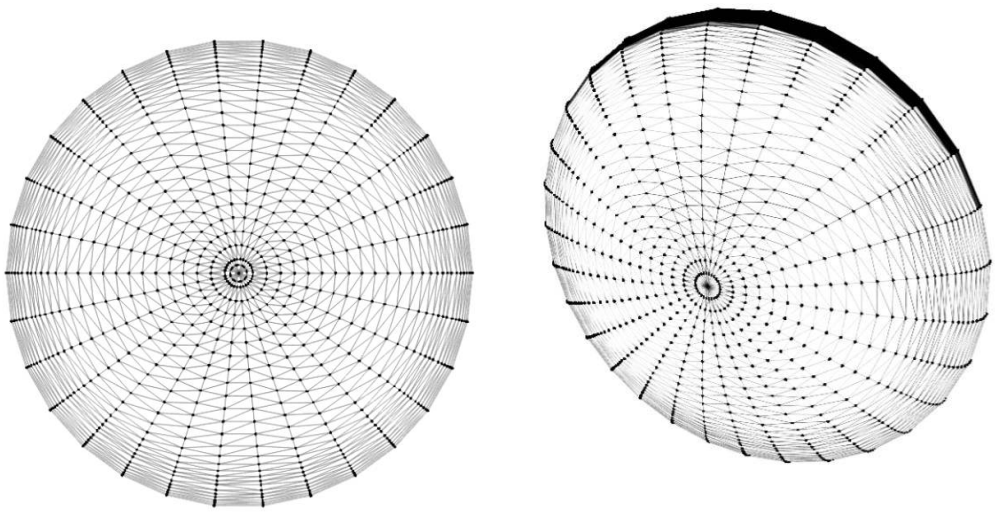

Figure 2. The surface mesh used for the Newtonian/axisymmetric analogue FIRE-II simulation.

Table 1. FIRE-II trajectory conditions selected for validation runs.[16]

t [s]	M [-]	h [km]	v km/s	ρ kg/m^3	T_∞ [K]	T_{wall} [K]	$Q_{\max}$ [W/cm^2] (CFD)	$Q_{\max}$ [W/cm^2] (Axisymm.)
1636	39.2	71.04	11.31	8.57E-05	210	810	183 - 365	180
1643	31.7	53.04	10.48	7.80E-04	276	640	769 - 904	501

The mesh that was used for the Newtonian/axisymmetric analogue FIRE-II simulation was created using Blender[b] and is shown in Figure 2. The two simulated points on the FIRE-II trajectory are summarised in Table 1, along with the reference CFD maximum heat flux results and the results of the current code.

The heat flux results at the 1636 s trajectory point are shown in Figure 3, where the predictions from the Newtonian/axisymmetric analogue method are compared with a variety of CFD simulation data.[7] The CFD simulations from the reference differ primarily in the way in which the chemistry is accounted for and are included to showcase the range of uncertainty that still exists for this test case, even with tools as accurate as CFD. When this is taken into account, the performance of the Newtonian/axisymmetric analogue solver can be considered decent. The flux is obviously lower than that coming other heat flux contributions. The points are generally around 30% below the lowest CFD prediction, and three to four times lower than the highest one, which is consistent with later findings, as will be shown in Sec. VI.

The initial flux in the front of the vehicle is resolved to be larger than the other points, due to it being included in the stagnation ϵ zone. Locally, the heat flux is in some places also underpredicted compared to the average profile, most likely due to the erroneously backtraced nodes, as discussed in the previous paper.[1] In general, however, the trend matches the FIRE-II CFD data well.

While for the FIRE-II test case, multiple CFD predictions exist to which the current technique can be compared, such as those seen in Figure 3, this is not the case for the DART configurations, which are the focus of this paper. To later perform an accuracy analysis and adjustment of the current method when applied to those configurations, a CFD model must developed to create the reference data. Before its application to the DART shapes, its validation against the FIRE-II data is briefly described.

To develop the CFD model, the COOLFluiD (Computational Object-Oriented Libraries for Fluid Dynamics) platform is used, since it has been already validated for hypersonic simulations[8] and uses a very stable implicit scheme. The PLATO thermochemical library, see, *e.g.,* Ref. 9, is used in combination with COOLFluiD to compute the chemistry and the reaction kinetics with the 11-species air model. The geometry is 2D and has 5,555 points and 5,400 elements.

The results and validation of the COOLFluiD platform for simulation of the FIRE-II mission, including

[b] https://www.blender.org/

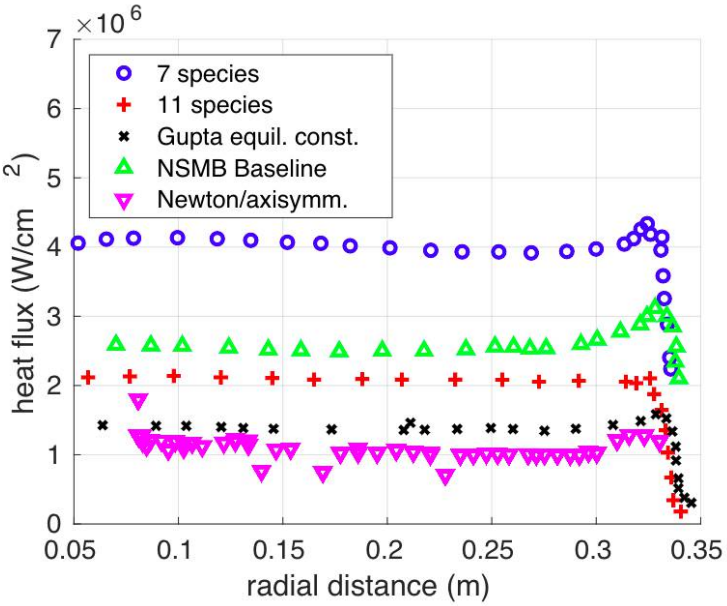

Figure 3. The heat flux over the FIRE-II test vehicle according to CFD simulations with various setups taken from Ref. 7 (7 species chemistry: blue "o", 11 species chemistry: red "+", chemistry with Gupta's equilibrium constant model: black "x", the NSMB baseline: green "Δ") and the current method (violet "∇").

the radiative heat flux, can be found in papers by Lani et al.[8] and Santos and Lani.[17] Originally, COOLFluiD was coupled with the Mutation thermochemistry library from the Von Karman Institute. Recently, effort has been invested to couple COOLFluiD with the PLATO (PLAsmas in Thermodynamic nOn-equilibrium) thermochemistry library developed at the University of Illinois.[18] This library will also be used in this paper. Thus, since the validation of COOLFluiD with the FIRE-II case was performed with the Mutation library, this run was replicated for the 1643 s trajectory point and compared to the reference results from the paper of Goebel and coworkers in Ref. 7. Since otherwise the CFD setup was the same as in Refs. 8 and 17, and there are constraints on the extent of this paper, it will not be elaborated on in further detail. The flowfield pressure and temperature as resolved by COOLFLuiD coupled with PLATO is shown in Figure 4. Qualitatively, the flowfield corresponds well to the previously published figures.[8] The shock is a well resolved layer with temperatures of up to 22,000 K. This temperatue was compared to the reference data from Ref. 7 in Figure 5. From Figure 5, it can be seen that the predicted temperatures of the shock are higher just like the shock stand off distance in case of the developed CFD model. However, this difference is still well within the normal range of what is expected between the different CFD solvers for this case using different thermochemical libraries (see *e.g.,* , Ref. 17, where the peak temperature is only 12,000 K compared to the reference 18,000 K from Ref. 7). In addition, the post-shock values are in a very good match with the reference data. Thus, this CFD setup will be further used also in this paper to produce reference data for the analysis and correction of the modified Newtonian/axisymmetric analogue technique.

IV. Further Leeward Accuracy Improvements

Previously, on the leeward side of the geometry, the pressure coefficient was defined as $-1/M^2$. To increase the accuracy of the computation of the pressure forces, for which the leeward pressure coefficient is also important, the following formula established by Gabeaud[19] is now employed:

$$C_{p,b} = \frac{2}{\gamma M_\infty^2}\left\{\left(\frac{2}{\gamma+1}\right)^{1.4}\left(\frac{1}{M_\infty}\right)^{2.8}\left[\frac{2\gamma M_\infty^2-(\gamma-1)}{\gamma+1}\right]-1\right\} \tag{16}$$

To visualise the importance of this addition, one of the trajectories from the previous study (nominal trajectory of configuration 10) was revisited and the change to the drag force due to the change in the leeward pressure coefficient was computed. The results are shown in Figure 6, from which it can be clearly

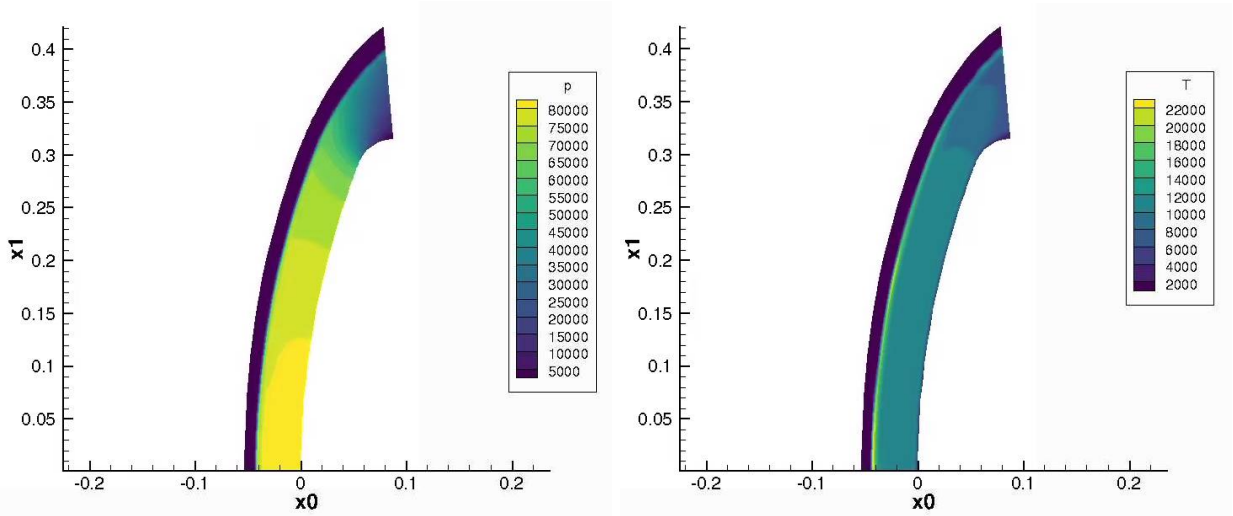

Figure 4. The FIRE-II flowfield at 1643 s as resolved by the developed COOLFluiD CFD model.

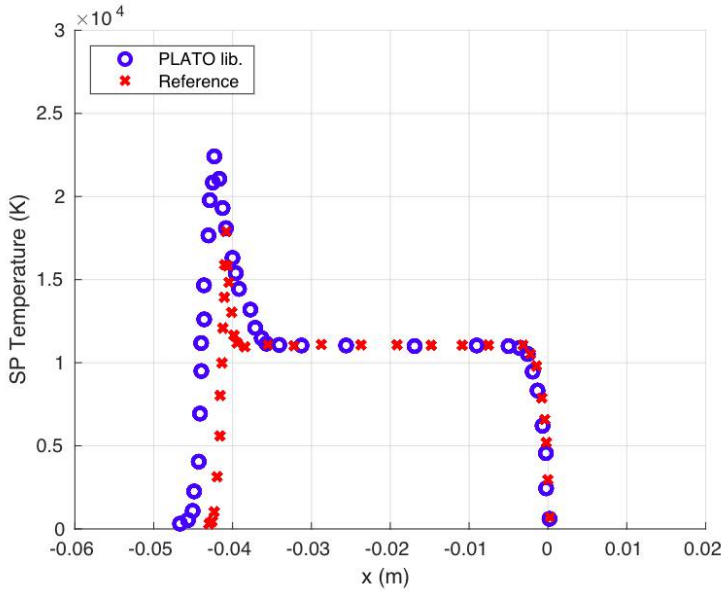

Figure 5. Comparison between stagnation line temperature profiles of reference data from Ref. 7 and results obtained with the developed CFD model.

observed that especially later during the flight at lower Mach numbers, this difference is quite substantial, representing nearly a third of the entire drag force that the vehicle experiences.

V. Design Optimisation Configuration

Just like in the previous paper,[1] the object for optimisation is the biconic DART module already studied by Sudmeijer and Mooij in 2002,[10] where the main variables are the nose radius, R_N, the semi cone-angle, θ_c, the semi flare-angle, θ_f, the vehicle length, L, and the base radius, r_B (see Figure 7(a) for the parameters and 7(b) for the nominal configuration). By varying all five parameters, for the range of variation applied, the geometric constraints will be violated by one of the designs. One way to solve this is to limit the maximum range, but this will result in only small differences in between configurations. Therefore, we will restrict to a variation in four parameters, and constrain the base radius to a fixed value of $r_B = 0.56$ m. Thus, different

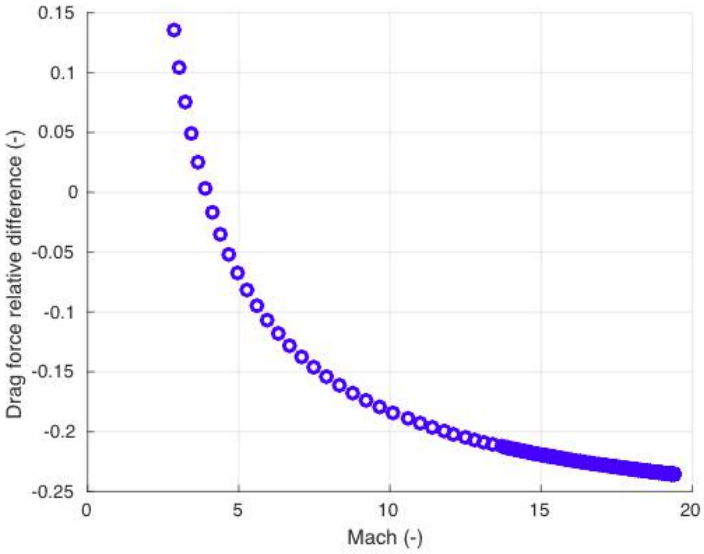

Figure 6. Example relative drag difference for one of the configurations on its nominal trajectory due to the implementation of the improved leeward pressure coefficient estimate as a function of the Mach number.

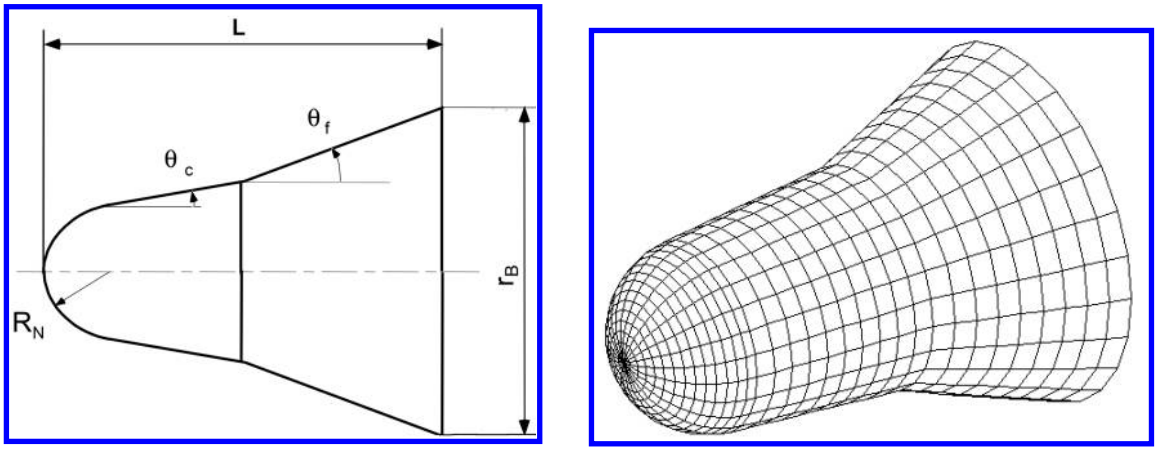

(a) Geometry (b) Nominal configuration

Figure 7. The biconic DART capsule configuration showcasing the geometrical parameters for variation.

configurations are generated for this study to allow for a complete response-surface optimisation process and not only a comparison of heat fluxes, as presented before. The configurations considered are visualised in Figure 8, with the corresponding numerical values of the geometric parameters shown in Table 2.

Each evaluation requires the generation of a vehicle surface mesh, an aerodynamic analysis (using the Newtonian/axisymmetric model), a simulation of the ballistic trajectory, and the computation of several objectives along this trajectory. These objectives are, amongst others, the heat flux at three different locations on the vehicle and the maximum *g-load*. Initial conditions, with the vehicle mass m = 200 kg, at h = 120 km for this ballistic trajectory are a velocity of V_0 = 5,250 m/s, a flight-path angle of γ_0 = -6.5° with the longitude and latitude arbitrarily zero-initialised. The entry flight is along the equator in eastward direction, so the heading is $\chi_0 = 90°$.

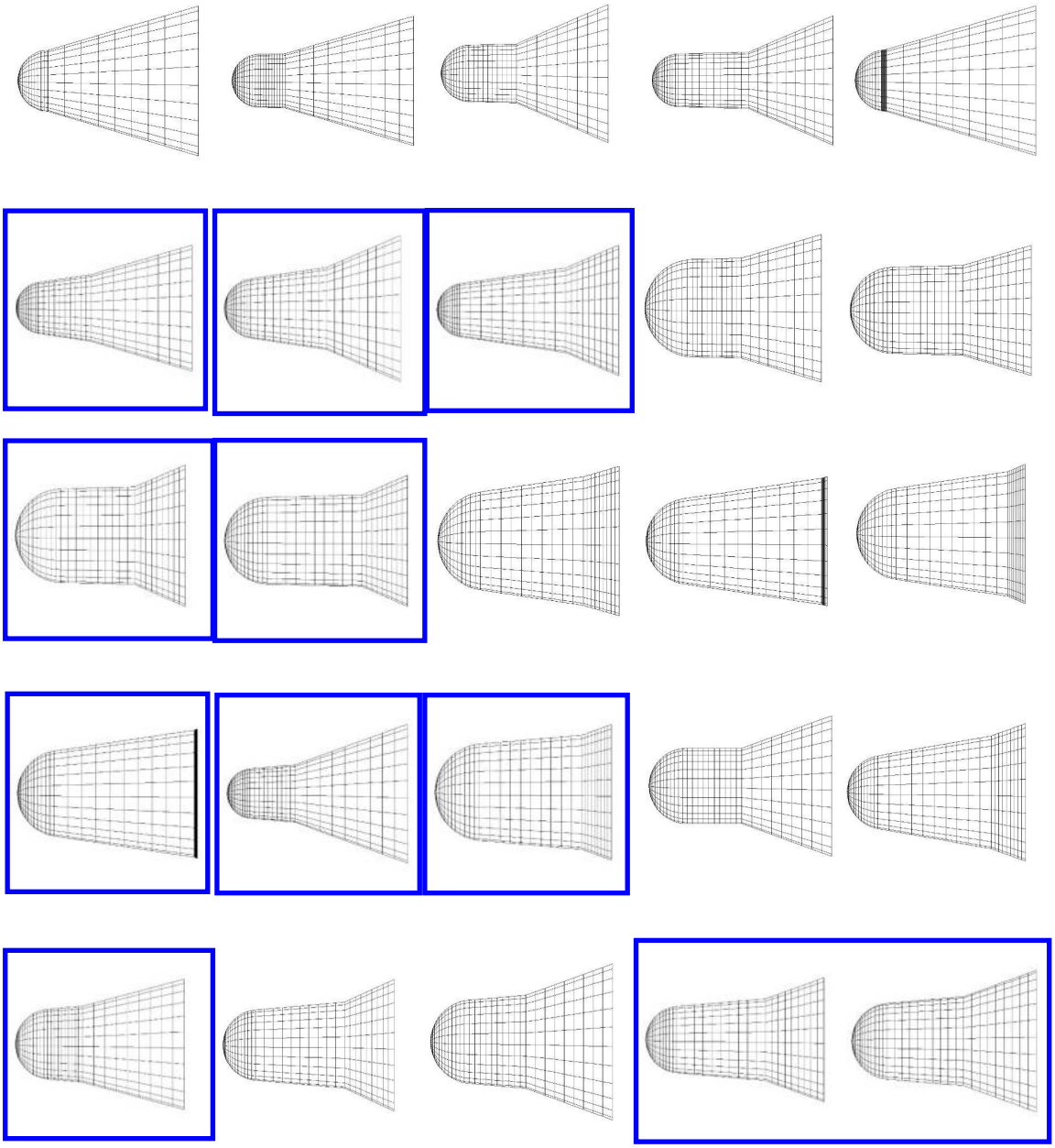

Figure 8. DART geometric configurations selected for response surface shape optimisation.

VI. Assessment of Heat-Flux Accuracy

A. Simulation Specifications

The CFD simulations to estimate the thermal and chemical error in the heat flux were ran at the points at which, according to the axisymmetric calculations, the aerodynamic heat flux was roughly the highest. This way, the uncertainty would be determined at the most critical point of the trajectory to which the design of the TPS system is usually the most sensitive. The conditions of the CFD simulation for each of the configurations are summarised in Table 3. They were ran in the laminar regime to prevent further turbulence-model related uncertainties and thus naturally, also the corresponding axisymmetric calculations for comparison were forced to remain laminar as well.

Table 2. Central Composite Design of the biconic re-entry capsule with parameters.

	Design	R_N (m)	θ_c (°)	θ_f (°)	L (m)
1	L16 row #01	0.229	1.464	16.464	1.344
2	L16 row #02	0.229	1.464	16.464	1.556
3	L16 row #03	0.229	1.464	23.536	1.344
4	L16 row #04	0.229	1.464	23.536	1.556
5	L16 row #05	0.229	8.536	16.464	1.344
6	L16 row #06	0.229	8.536	16.464	1.556
7	L16 row #07	0.229	8.536	23.536	1.344
8	L16 row #08	0.229	8.536	23.536	1.556
9	L16 row #09	0.371	1.464	16.464	1.344
10	L16 row #10	0.371	1.464	16.464	1.556
11	L16 row #11	0.371	1.464	23.536	1.344
12	L16 row #12	0.371	1.464	23.536	1.556
13	L16 row #13	0.371	8.536	16.464	1.344
14	L16 row #14	0.371	8.536	16.464	1.556
15	L16 row #15	0.371	8.536	23.536	1.344
16	L16 row #16	0.371	8.536	23.536	1.556
17	-Axial #01	0.200	5.000	20.000	1.450
18	Axial #01	0.400	5.000	20.000	1.450
19	-Axial #02	0.300	0.000	20.000	1.450
20	Axial #02	0.300	10.000	20.000	1.450
21	-Axial #03	0.300	5.000	15.000	1.450
22	Axial #03	0.300	5.000	25.000	1.450
23	-Axial #04	0.300	5.000	20.000	1.300
24	Axial #04	0.300	5.000	20.000	1.600
25	centre point	0.300	5.000	20.000	1.450

B. Thermal Heat Flux

Two types of heat flux profiles were derived from the CFD data; the thermal heat flux and the chemical heat flux. In this subsection, first, the modelled thermal heat flux deviations are addressed; the handling of the unmodelled chemical heat flux contributions will be discussed in the section following.

An example comparison between the CFD thermal heat flux data and the axisymmetric data, here for the 4th configuration, are shown in Figure 9. The first apparent difference between the profiles is the heat flux very close to the nose. Here, this value is much larger for the axisymmetric estimate. The most likely reason for this is the fact that the formula used to derive this value applies to the stagnation point directly (see the theory explain in Ref. 1). This is a theoretical value somewhere in the flow, not exactly at the nose wall. Some of the energy will be lost at the nose compared to the stagnation point and thus the CFD wall values are lower.

It was thus attempted to evaluate this difference for all the configurations, as it was fairly consistent. The relative difference $\frac{q_{\text{axis}}-q_{\text{CFD}}}{q_{\text{axis}}}$, is plotted in Figure 10, with the nose radius on the x axis, as it was expected that this error would be a function of the nose geometry. While a certain trend is definitely visible, it would be difficult to justify any type of a fitting function that could be used instead with nose radius as a parameter only due to the data spread. Thus, these corrections were taken directly per configuration from the CFD comparison and fed back into the axisymmetric solver.

Another difference observed in Figure 9 is in the the heat flux transition from the nose into the cone area (*ca.* 0.2 m to 0.5 m). In these regions, also for the other configurations, it was observed that the axisymmetric analogue method almost always underpredicted the heat flux. Since this is the location of the conical part which experiences the highest heat flux (right at the junction with the nose), again, the error was estimated for each configuration separately and fed back into the axisymmetric analogue script.

Finally, the heat flux profile at the end of the flare should be addressed, where flow expansion takes place. While this mostly affects chemical fluxes, as seen in Figure 9, a small local increase can also be observed in the thermal heat-flux profile.

Table 3. Conditions for each configuration used as an input for the CFD simulations.

Config	h [km]	V_∞ [m/s]	M_∞ [-]	T_∞ [K]	ρ_∞ [$\frac{kg}{m^3}$]	ρ_∞(N) [$\frac{kg}{m^3}$]	ρ_∞(O) [$\frac{kg}{m^3}$]
1	3.629E+01	4.511E+03	1.452E+01	2.401E+02	6.943E-03	5.322E-03	1.620E-03
2	3.536E+01	4.431E+03	1.434E+01	2.375E+02	8.007E-03	6.138E-03	1.869E-03
3	3.845E+01	4.484E+03	1.426E+01	2.461E+02	5.017E-03	3.846E-03	1.171E-03
4	3.845E+01	4.489E+03	1.428E+01	2.461E+02	5.023E-03	3.850E-03	1.172E-03
5	3.536E+01	4.429E+03	1.434E+01	2.375E+02	8.003E-03	6.135E-03	1.868E-03
6	3.531E+01	4.460E+03	1.444E+01	2.374E+02	8.067E-03	6.184E-03	1.883E-03
7	3.746E+01	4.447E+03	1.422E+01	2.433E+02	5.817E-03	4.460E-03	1.358E-03
8	3.737E+01	4.500E+03	1.440E+01	2.431E+02	5.896E-03	4.520E-03	1.376E-03
9	3.959E+01	4.437E+03	1.402E+01	2.492E+02	4.245E-03	3.254E-03	9.908E-04
10	3.958E+01	4.440E+03	1.403E+01	2.492E+02	4.249E-03	3.257E-03	9.916E-04
11	4.064E+01	4.432E+03	1.392E+01	2.521E+02	3.641E-03	2.791E-03	8.498E-04
12	4.063E+01	4.437E+03	1.394E+01	2.521E+02	3.646E-03	2.795E-03	8.510E-04
13	3.951E+01	4.479E+03	1.416E+01	2.490E+02	4.291E-03	3.289E-03	1.002E-03
14	3.857E+01	4.418E+03	1.404E+01	2.464E+02	4.931E-03	3.780E-03	1.151E-03
15	3.870E+01	4.345E+03	1.380E+01	2.468E+02	4.837E-03	3.708E-03	1.129E-03
16	3.858E+01	4.411E+03	1.402E+01	2.464E+02	4.922E-03	3.773E-03	1.149E-03
17	3.634E+01	4.484E+03	1.443E+01	2.402E+02	6.896E-03	5.286E-03	1.609E-03
18	4.059E+01	4.461E+03	1.402E+01	2.520E+02	3.668E-03	2.812E-03	8.561E-04
19	3.852E+01	4.443E+03	1.412E+01	2.463E+02	4.964E-03	3.806E-03	1.159E-03
20	3.745E+01	4.454E+03	1.424E+01	2.433E+02	5.828E-03	4.468E-03	1.360E-03
21	3.863E+01	4.382E+03	1.392E+01	2.466E+02	4.885E-03	3.745E-03	1.140E-03
22	3.951E+01	4.480E+03	1.416E+01	2.490E+02	4.292E-03	3.290E-03	1.002E-03
23	3.848E+01	4.467E+03	1.420E+01	2.462E+02	4.995E-03	3.829E-03	1.166E-03
24	3.844E+01	4.494E+03	1.429E+01	2.460E+02	5.029E-03	3.855E-03	1.174E-03
25	3.846E+01	4.480E+03	1.425E+01	2.461E+02	5.011E-03	3.842E-03	1.170E-03

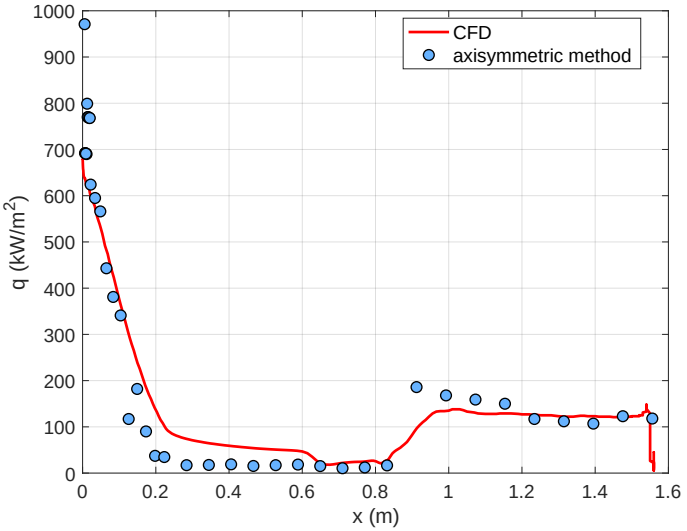

Figure 9. An example comparison between the thermal heat flux predictions coming from the CFD (black squares) and the modified Newtonian/axisymmetric analogue method (blue triangles) for the 4th configuration over its length, at the point of the trajectory of maximum aerodynamic heating.

As the axisymmetric analogue technique cannot model this flow expansion properly, this represents an additional correction that will have to be made to the heat-flux figures used for optimisation, especially since this region is usually the region of the highest flare heat flux. The average heat flux over the end section of the flare was evaluated and compared to the peak heat flux at its very end. The results are shown in Figure

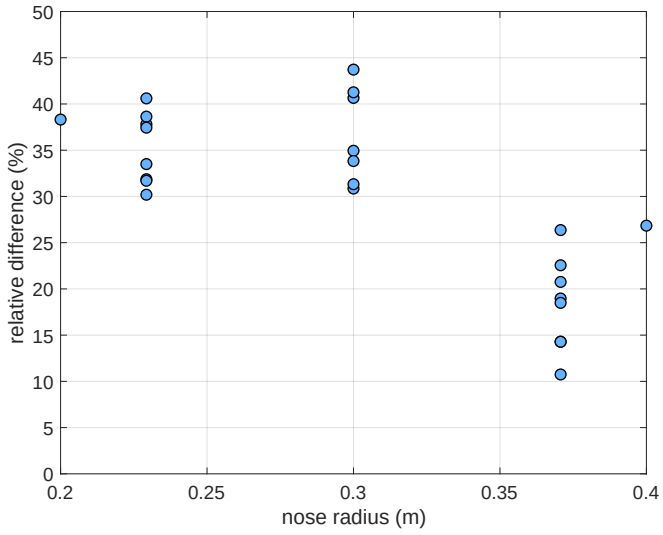

Figure 10. The relative difference $\frac{q_{\mathbf{axis}}-q_{\mathbf{CFD}}}{q_{\mathbf{axis}}}$ between the theoretical stagnation point heat flux and the actual maximum heat flux on the nose wall determined from CFD, here shown as a function of the nose radius.

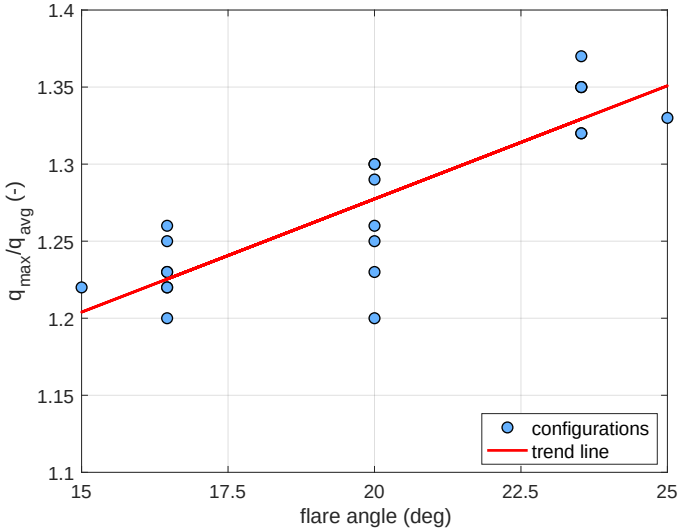

Figure 11. The ratio of the maximum thermal heat flux to the average thermal heat flux over the aft portion of the vehicles from the CFD simulations, as a function of the flare angle with respect to the freestream.

11 as a function of the total flare angle with respect to the freestream. A roughly linear trend is observed, and used as the last correction to the thermal heat-flux output from the solver.

C. Overall Heat Flux

Now that the deviations in the thermal heat flux were assessed, the components of the heat flux which cannot be modelled by the solver must be estimated. In these simulations (at conditions of the largest aerodynamic heating), the chemical heat flux is actually the dominant component (and the radiative heat flux was neglected). The chemical and the thermal heat fluxes were compared for each configuration along the profile of the vehicle. The ratio of the total heat flux $q_{tot} = q_c + q_{th}$ to the thermal heat flux q_{th} is shown in Figure 12 for the first 12 configurations and Figure 13 for the remaining 13 configurations. Note that in

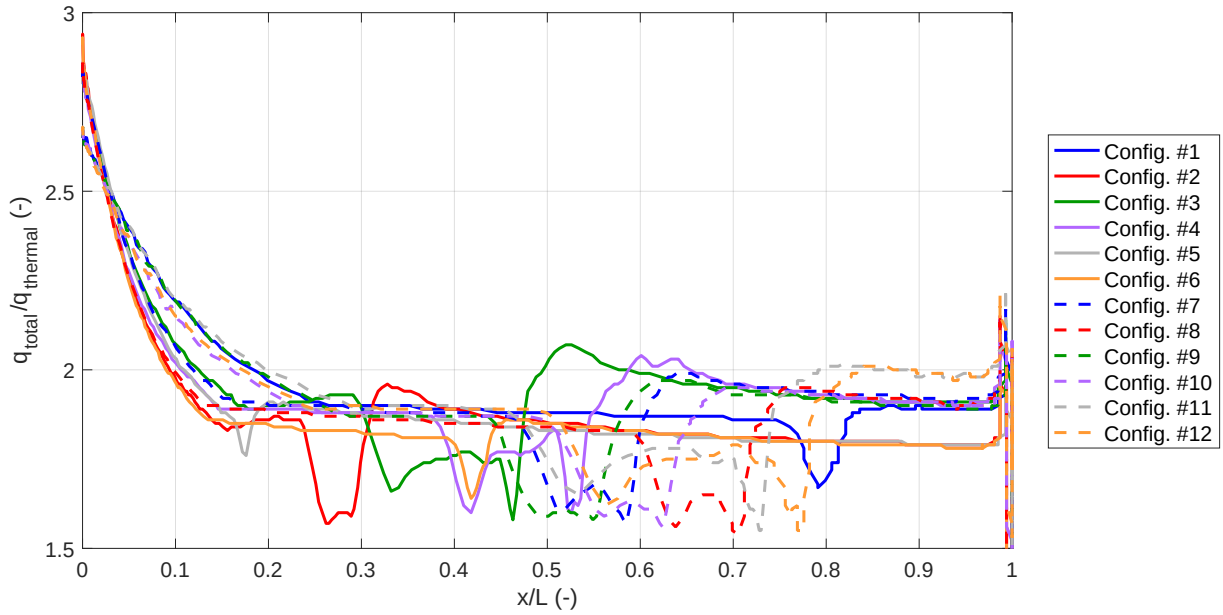

Figure 12. The ratio of the total heat flux to the thermal heat flux for configurations 1 through 12, as a function of the position along the vehicle normalised by its length.

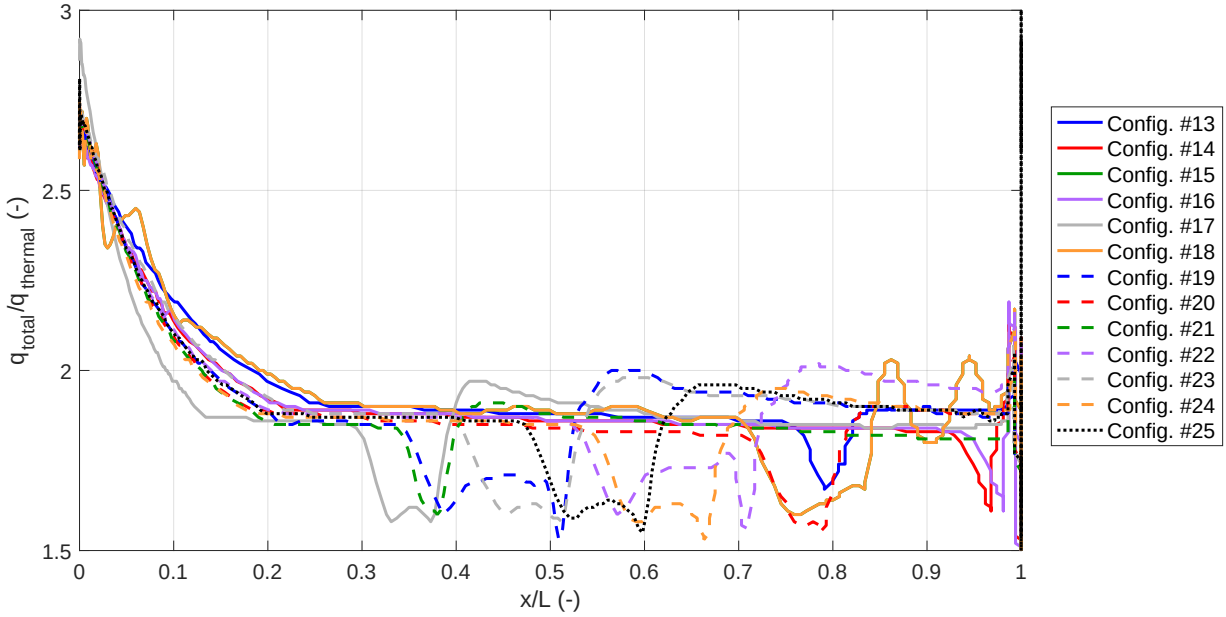

Figure 13. The ratio of the total heat flux to the thermal heat flux for configurations 13 through 25, as a function of the position along the vehicle normalised by its length.

Figures 12 and 13, the relative length is used so that the configurations of different lengths can be compared.

Several trends can be observed. Firstly, the ratios over the nose component between the various geometries are very similar, starting from 2.7 to 2.9 and decreasing down to around 1.8 to 1.9, where the conical section starts. Secondly, the ratio after this zone then varies depending on the particular geometry. It decreases down to around 1.6 to 1.7 in the aft part of conical section before the start of the flare. Finally, in the flare, it generally stays between 1.9 to 2.0, apart from the aft spot, which was already addressed in the previous section. It can be noted that these heat-flux errors agree very well with the deviation that was also observed

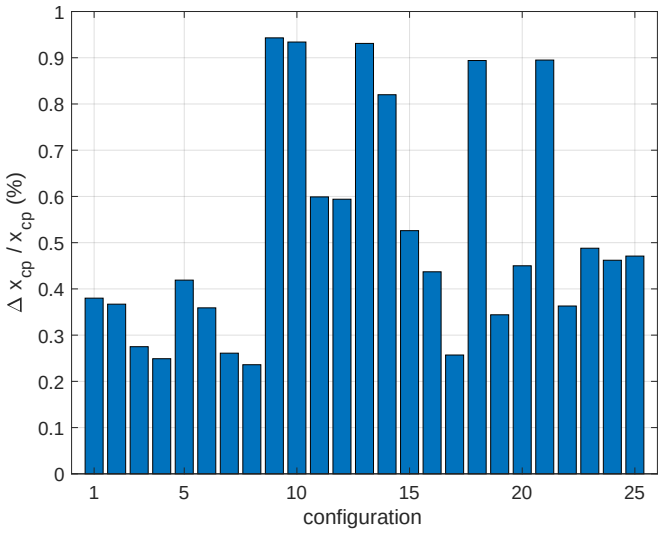

Figure 14. The relative movement of the centre of pressure of each configuration during the simulated nominal trajectory, with its average distance taken as a normalisation factor.

for the FIRE-II simulation in Sec. III. From Figures 12 and 13, the factors for corrections of the thermal heat flux were determined. For the maximum nose-, cone- and flare heat flux, the factors of 2.75, 1.8 and 2.0 were chosen, respectively.

It is obvious that these correction factors do not hold for the entire trajectory, as the significance of the chemical effects varies considerably during the flight. For example, at Mach numbers closer to 10, the chemical effects were found to be almost negligible. They were, nevertheless, included in this form, since the peak heat fluxes, for which these correction factors were determined, are one of the main targets for the optimisation process and are very sensitive for the vehicle design.

While these factors can represent a good and a practical correction technique for the optimisation parameters of the maximum heat fluxes, it must be noted that their value also impacts the integrated heat load. Since they were derived at one trajectory point only and then applied in the same way for all of the trajectory points when this integration was taking place, it is likely that their inclusion made the integrated heat load figure less accurate, and probably much higher. This should be considered when interpreting the results of the optimisation process and will be addressed in the recommendations.

VII. Axisymmetric Simulation Specifications

With the correction factors determined, the axisymmetric calculations were re-ran. For each of the 25 configurations, a full trajectory was simulated from 120 km down to around 20 km, with a 1-second temporal resolution. The maximum heat flux overall in each section was identified and corrected. In addition, in each section, the corrected heat flux at the location where it was at its maximum was also integrated over time to arrive to the integrated heat load. As mentioned previously, while the calculations above considered laminar flow only, to create inputs into the optimisation procedure, turbulent flow was assumed with a natural transition position determined by the criteria stated in Ref. 1.

Finally, the centre of pressure was also determined for each configuration. Since the pressure coefficient at the aft section of the vehicle depends on the Mach number, the location of this centre of pressure is not a constant and varies over the trajectory. Nonetheless, this variance was found to be relatively small and shift aft consistently with the increasing Mach number. The relative error due to this variation (*i.e.,* the size of the movement over the average distance) for each configuration is shown in Figure 14. Since this does not exceed 1%, which is far less than the expected accuracy of the Newtonian pressure coefficient, it justifies assuming a constant location of the centre of pressure during the optimisation process.

With the heat fluxes corrected and determined along with the integrated heat load and the centre of pressure, the design optimisation could take place, results of which are presented in the next section.

VIII. Design Optimisation Results

As we discussed before, with four design parameters a central composite design with 25 configurations is performed. The resulting configurations listed in Table 2, and visualised in Figure 8, were all meshed and run through the axisymmetric code. The free-stream conditions for the point of maximum thermal loads were taken from the corresponding trajectories that were obtained with the use of simplified modified Newtonian aerodynamics. It was established earlier that using the improved aerodynamics has a marginal effect on the hypersonic trajectories for ballistic flight.[1]

Having obtained the response values for the maximum heat flux on the nose, the cone and the flare, as well as the corresponding surface-integrated heat load and the location of the centre of pressure, the fitting process could begin. After the first trials it was clear that the second-order model Eq. (11) was not always the best fit. To better understand the dependencies on the independent parameters, analysis of variance (ANOVA) is done on the factorial portion of the design[c].

Because there is an equal number of experiments n_k at each of the levels for one factor x_j when they are varied according to an orthogonal array, it is easy to compute the factor sum of squares, S_j. The sum of squares S_j for factor x_j on levels $x_{j,k}$ is the sum of all level variations:

$$S_j = \frac{1}{n_L} \frac{\left(\sum^{N} y(x_j^+) - \sum^{N} y(x_j^-) \right)^2}{n_k} \tag{17}$$

with each sum adding all responses at level k (+1 or -1) together (n_k out of the total of N samples); n_L is the number of levels ($n_L = 2$ for the linear variations considered in the CCD). This factor sum of squares can be used to assess the response sensitivity to a particular factor variation by determining the corresponding relative contribution to S_T:

$$P_j = \frac{S_j}{S_T} * 100\% \tag{18}$$

The error sum of squares S_E is simply the difference between S_T and the sum of all S_j (j = 1,...,k). Note that so-called interaction tables determine on which columns the interactions are "acting", *e.g.,* column #3 of the L_{16} array represents the interaction between the first and second column (design parameters R_N and θ_c). Thus, with the same Eq. (17) the interaction contribution can be determined.

Doing the ANOVA for the heat-load and heat-flux related responses gives the results shown in Figure 15. The figure shows that the responses for the nose and flare are mainly driven by the linear factor effects (apart from quadratic terms that are not shown here), but in case of the cone there are higher-order interaction effects at play, for instance, an interaction $x_1 \times x_2 \times x_3$. This shows as a 20% error term, which includes all unmodelled interactions. The cone flux is thus not easily modelled with the second-order model, and additional terms need to be included.

After some trials the following terms to compute the response surfaces were included. For the nose, the two responses were modelled with all linear (x_1, *etc.*) and quadratic (x_1^2, *etc.*) terms, as well as $x_1 \times x_2$, $x_2 \times x_3$, and $x_2 \times x_3 \times x_4$. The cone-related responses have been modelled with all linear, quadratic, and cubic terms (*e.g.,* x_1^3), as well as the higher-order interaction $x_1 \times x_2 \times x_3$. Finally, the flare was modelled with the standard second-order model, but extended with all cubic terms. This model was also used for the centre-of-pressure location, although this response did not show so much variation, as was already established (Figure 14).

Solving for the coefficients of the response surfaces and evaluating the 25 configurations yielded the fitted responses shown in Figure 16, with coefficients of determination of R_A^2 = 0.7610, 0.8905, 0.8391, 0.7508, 0.9347, and 0.8540 for the six thermal-load related responses. The centre-of-pressure location showed an excellent fit with R_A^2 = 0.9971. Overall, the fits are quite accurate.

The next step in the process is to optimise the configuration by using the response surfaces (using the goal-attainment algorithm of the Optimization Toolbox of Matlab). However, here we are faced with a potential issue. Since in the current study the thermal data are matched with the CFD results (that were

[c]Due to the structure of the orthogonal array that represents this fractional factorial part, ANOVA is a straightforward process.[23] One can then identify the main contributions to the total sum of squares of the linear and interaction terms. However, because the (normalised) variables are changed over two levels only, *i.e.,* -1 (minimum) and +1 (maximum), quadratic effects cannot be established.

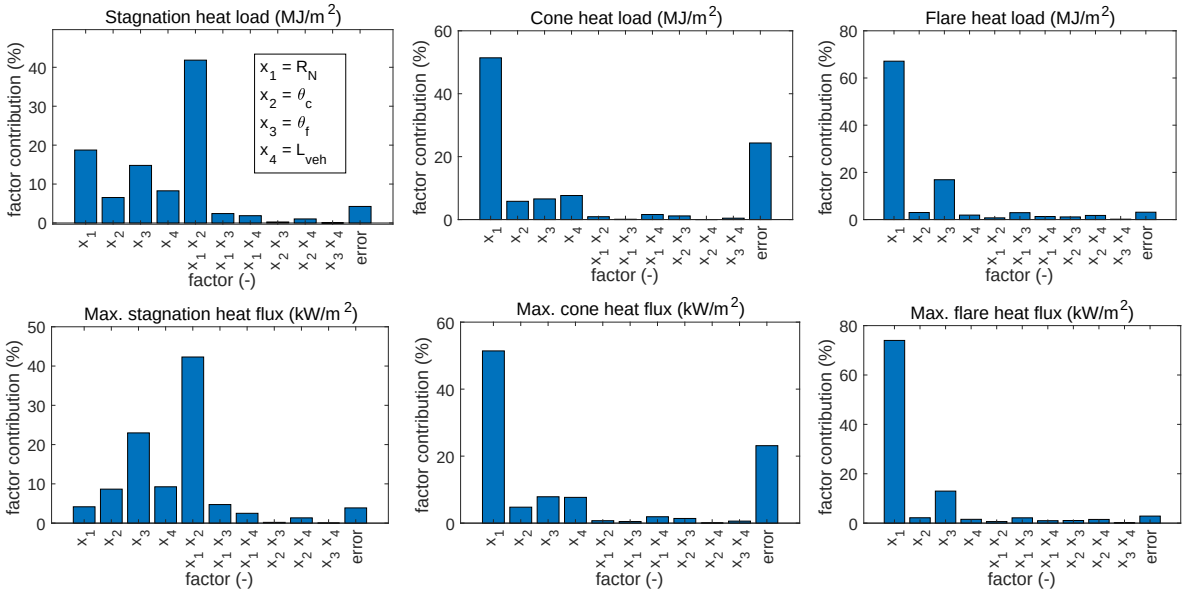

Figure 15. Main factor and interaction contribution to the total sum of squares.

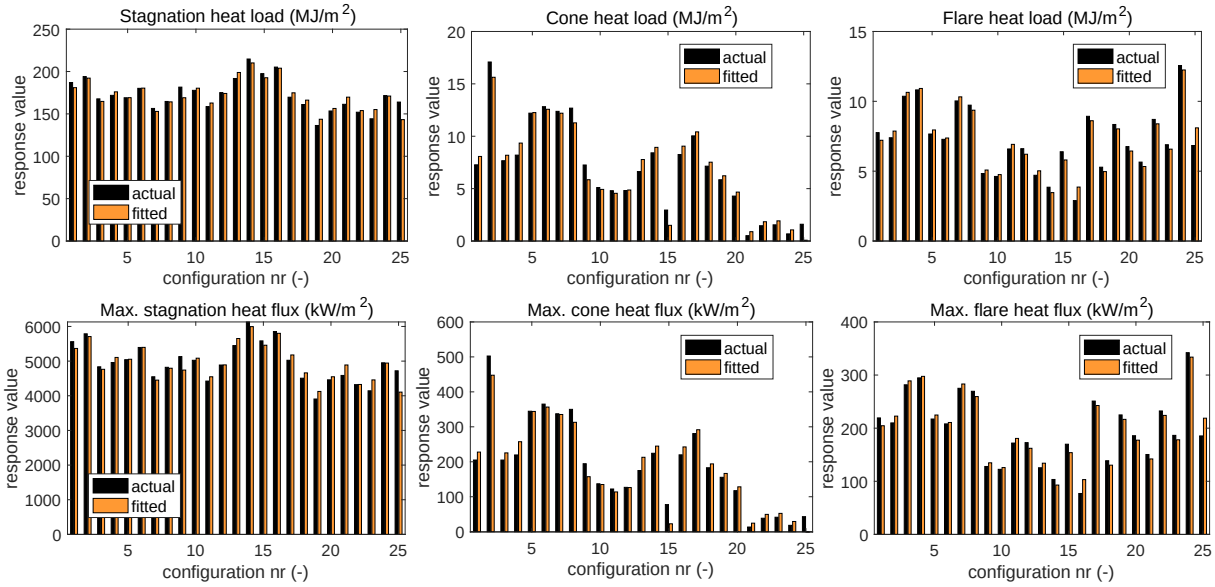

Figure 16. The six thermal-load related responses, both the actual input and the fitted data.

available as part of the validation process), the optimised configuration requires correction factors that are not available, because for the optimised shape no CFD data are yet produced. However, we could try to estimate the correction factors by fitting the factors that we have and use the corresponding response surfaces to predict these correction factors. This seems to be a reasonable approach, but care should be taken while interpreting the results.

The correction factors for nose and flare are plotted in Figure 17, obtained with inclusion of all linear and quadratic terms, as well as $x_1 \times x_2$, $x_2 \times x_3$, and $x_2 \times x_3 \times x_4$ (nose), and the second-order model of Eq. (11) extended with $x_1 \times x_2 \times x_3$ for the flare. The cone correction-factor is taken as constant, and equal to 2.0.

The optimal configuration was found to be: $R_N = 0.353$ m, $\theta_c = 0°$, $\theta_f = 18.83°$, and $L = 1.43$ m, with maximum flux values of $q_{c,nose} = 3842$ kW/m^2, $q_{c,cone} = 267$ kW/m^2, and $q_{c,flare} = 170$ kW/m^2.

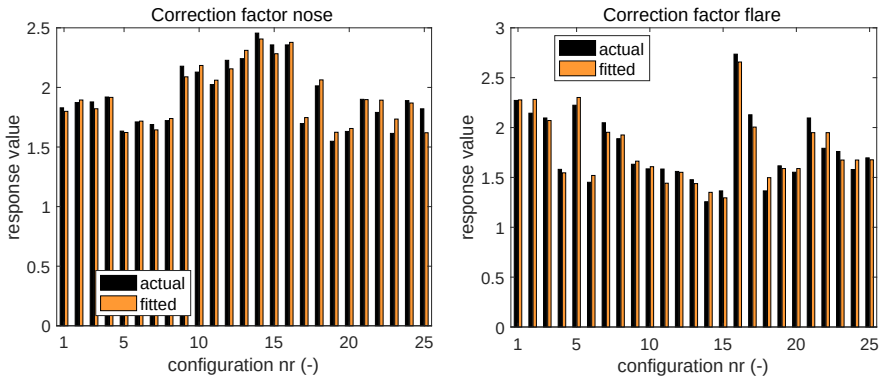

Figure 17. The actual and fitted correction factors for nose and flare, with $R_A^2 = 0.8689$ and 0.8382, respectively.

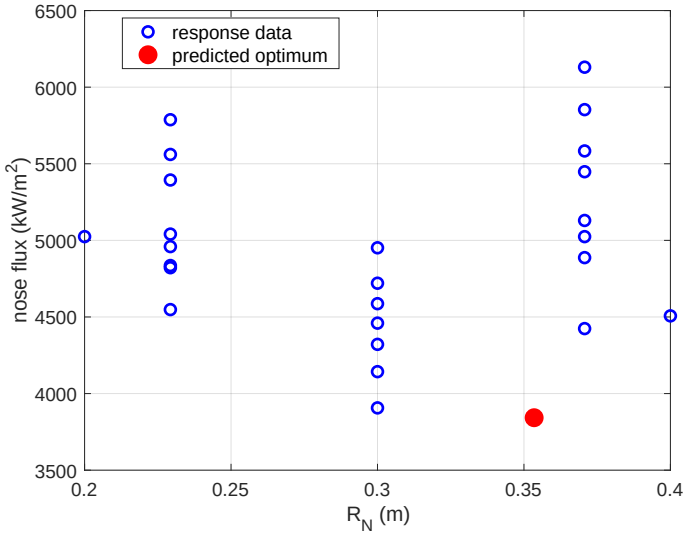

Figure 18. Response data for the nose flux, including the found optimum.

Comparing, for instance, the nose flux with the response data (Figure 18), we see that the predicted value is on the low side, although not infeasibly low.

To verify the correctness of the final fluxes which came from the optimisation process, the Newtonian/ axisymmetric code was re-run with the final geometry. This was, however, not sufficient, since the optimisation methodology also considered the CFD corrections. As discussed above, the correction factors followed from the response surfaces as well, and had the values of 1.6, 2.0, 1.5 for the nose, cone and flare, respectively (in which the thermal and the chemistry effects were already combined).

Considering these adjustments to the results from the Newtonian/axisymmetric method, the final fluxes for the optimised configuration were 4181.33 kW/m^2 for the nose, 283.47kW/m^2 for the cone and 239.27kW/m^2 for the flare. Overall, the verified fluxes are somewhat larger than predicted, but not overly so. A combination of reasons may be underlying this difference: the response surface may be a bit oscillatory in between the nodal points, the correction factors determined are not 100% accurate, and there may be some unmodelled higher-order effects at play. These aspects should be taken into account in future research.

Obviously, here, the comparison between the two sets of fluxes is not completely objective as the corrections to these fluxes came from the optimisation process itself, accuracy of which is aimed to be assessed, and these corrections represent a large fraction of the final fluxes. In the future, it should be attempted to evaluate these results for an optimal configuration for which the CFD data are also available. This was, however, not possible here due to time constraints.

Concluding, with all limitations involved, it seems that the response-surface methodology in combination with the Newtonian/axisymmetric analogue technique can potentially be a valuable tool during design-space exploration in the conceptual-design phase. Some potential improvements to this methodology are discussed among recommendations in the next section.

IX. Conclusions and Recommendations

This paper presents the application of the Newtonian/axisymmetric analogue technique on design optimisation of the biconic DART module considering 25 different geometric configurations, while also taking heat-flux corrections, based on CFD, partly into account.

Following up the previous paper,[1] the optimisation of the DART module originally studied by Sudmeijer and Mooij in Ref. 10 was revisited, this time with all of the configurations geometrically feasible. Besides the full optimisation, it was also intended to further improve the accuracy of the method at hand using CFD data as a reference. Without modifications, this technique is unable to predict chemical heat flux contributions and also suffers from many inaccuracies due to it being based on the Newtonian method pressure estimate. Thus a CFD model was setup based on the COOLFluiD platform to provide reference data at the trajectory points of maximum heating and create correction factors for the Newtonian/axisymmetric method.

The FIRE-II testcase showed that the current method gives heat fluxes roughly 2 to 3 times lower than the CFD predictions, primarily due to its omission of the chemical contributions at the analysed trajectory points. This was actually consistent with what was also found with the developed CFD model when investigating the DART geometries later during the process. Additional error was found at the nose, since the current technique considers the theoretical stagnation point value to be the heat-flux value at the nose directly.

From the comparison with laminar CFD, correction factors were determined and applied back to the solver to scale its results. This was the physically most accurate way to predict the maximum heat fluxes over the trajectories, which is the one of the primary concerns for optimisation, as the vehicle design is very sensitive to it. However it also introduced errors into the integrated heat load, as these correction factors remained unaltered during the trajectory, even though they were derived for one trajectory point only.

In addition to the heat-flux corrections, also the leeward pressure-coefficient computation was made more accurate compared to the default Newtonian method. This was important for better estimating the centre-of-pressure location and thus the vehicle stability. However, it was found that for the studied configurations that the centre-of-pressure location was more or less constant.

The nominal trajectories of the 25 configurations were re-ran with the correction factors applied and the maximum heat fluxes, integrated heat loads and the pressure coefficient locations were fed to the design optimisation procedure. Through analysis of variance and response surface methodology, the heat load and the heat flux responses were obtained, also taking the chemical and thermal correction factors into account. This led to the determination of the most optimal design from the considered design space, of $R_N = 0.353$ m, $\theta_c = 0°$, $\theta_f = 18.83°$, and $L = 1.43$ m. The same configuration was once again modelled with the Newtonian/axisymmetric code using the correction factors as fitted during the optimisation process. While the newly computed fluxes were a bit higher than predicted through optimisation, they still matched fairly well. To improve the reliability of this verification, it is recommended to gather additional CFD data for this final configuration. From a response-surface point of view, it may be worthwhile to try to establish a third-order design of experiments method to account for the unmodelled non-linearities in the problem at hand. For instance, a three-factor factorial design with four design parameters would require 81 design loops.

In the future, it might also be more beneficial to create a more spread database, over a variety of flight conditions, depending on which factor is more important for the vehicle design - the maximum heat flux or the integrated heat load. Then, for example, a method such as co-kriging could be used to better estimate these corrections at various points of the trajectory, so also at the points where the chemical effects are almost negligible. With the same number of CFD points, this approach would reduce the accuracy of the heat-flux estimation at the point of peak heating, but it would improve the accuracy of the estimate of the integrated heat load. In addition, it is the ultimate aim to make the methodology completely CFD-free. As was noted when evaluating the corrections, several trends have been observed which were consistent between the geometrically different configurations at similar flight conditions. Once these trends are studied in more detail, through more CFD simulations also at other trajectory points, it could be possible to formulate "rules of thumb" which can be applied universally (at least for concepts of a similar kind) and perform the whole calculation without any CFD requirements.

References

[1]Brchnelova, M. and Mooij, E. "Re-entry Shape Optimisation Using the Axisymmetric Analogue Method with Modified Newtonian Technique Resolved Inviscid Flow Field", AIAA 2021-0171, *AIAA SciTech Forum*, 19–21 January 2021, VIRTUAL EVENT.

[2]Cooke, J.C., "Axially Symmetric Analogue for General Three-Dimensional Boundary Layers", Reports and Memoranda No. 3200, British Aeronautical Research Council, 1961.

[3]Zoby, E.V. and Simmonds, A.L., "Engineering Flowfield Method with Angle-of-Attack Applications", *Journal of Spacecraft and Rockets*, Vol. 22, No. 4, 1985, pp. 398–404.

[4]Hamilton, H.H., DeJarnette, F.R., and Weilmuenster, K.J., "Application of Axisymmetric Analog for Calculating Heating in Three-Dimensional Flows", *Journal of Spacecraft and Rockets*, Vol. 24, No. 4, 1987, pp. 296-302.

[5]DeJarnette, F.R., Hamilton, H.H., Weilmuster, K.J. and Cheatwood, F.M., "A Review of Some Approximate methods Used in Aerodynamic Heating Analyses," AIAA-1985-0906, *AIAA 20^{th} Thermophysics Conference*, Williamsburg, Virginia, June 19-21, 1985.

[6]DeJarnette, F.R. and Hamilton, H.H., "Aerodynamic Heating on 3-D Bodies Including the Effects of Entropy-Layer Swallowing", *Journal of Spacecraft and Rockets*, Vol. 12, No. 1, 1975, pp. 5-12.

[7]Goebel, F., Vos, J. B., Mundt, Ch. "CFD Simulation of the FIRE II Flight Experiment", 42nd AIAA Fluid Dynamics Conference and Exhibit 25 - 28 June 2012, New Orleans, Louisiana

[8]Lani, A., Villedieu, N., Bensassi K., Kapa, L., Vymazal, M., Yalim, M. S. and Panesi, M. "COOLFluiD: an open computational platform for multi-physics simulation and research", *21^{st} AIAA Computational Fluid Dynamics Conference*, June 24-27, 2013, San Diego, California.

[9]Alberti, A., Munafò, A., Koll, M., Nishihara, M., Pantano, C., Freund, J. B., Elliott, G. S., and Panesi, M., "Laser-induced non-equilibrium plasma kernel dynamics," *Journal of Physics D: Applied Physics*, Vol. 53, No. 2, 2019, p. 025201.

[10]Sudmeijer, K.J. and Mooij, E., "Shape Optimisation for a Small Experimental Re-entry Module", AIAA-2002-5261, *AIAA/AAAF 11^{th} International Space Planes and Hypersonic Systems and Technology Conference*, 2002.

[11]Anderson, Jr., J.D., *Hypersonic and High-Temperature Gas Dynamics*, Second edition, AIAA Education Series, Reston, Virginia, 2006.

[12]Eckert E.R.C., "Engineering Relations for Heat Transfer and Friction in High-Velocity Laminar and Turbulent Boundary Layer Flows over Surfaces with Constant Pressure and Temperature", *Transactions of the American Society of Mechanical Engineering*, Vol. 78, No. 6, 1956, pp. 1273–1284.

[13]Parhizkar, H. and Karimian, S.M., "Application of Axisymmetric Analog to Unstructured Grid for Aeroheating Prediction of Hypersonic Vehicles", *International Journal of Numerical Methods for Heat and Fluid Flow*, Vol. 19, No. 3-4, 2009, pp. 501-520.

[14]Sutton K. and Graves, R.A., "A general stagnation-point convective-heating equation for arbitrary gas mixtures", NASA Technical Report R-376, 1971.

[15]Hamilton, H.H., Weilmuenster, K.J., and DeJarnette, F.R., "Approximate Method for Computing Convective Heating on Hypersonic Vehicles Using Unstructured Grids", *Journal of Spacecraft and Rockets*, 2014, Vol. 51, No. 4, 2014, pp. 1288-1305.

[16]Palmer, G. E., White, T., Pace, A. "Direct Coupling of the NEQAIR Radiation and DPLR CFD Codes", *10^{th} AIAA/ASME Joint Thermophysics and Heat Transfer Conference*, 28 June-1 July, 2010, Chicago, Illinois.

[17]Santos, P. D. and Lani, A., "An object-oriented implementation of a parallel Monte Carlo code for radiation transport", *Computer Physics Communications*, Vol. 202, 2016, pp. 233–261.

[18]Giangaspero, V. F., Lani, A., Poedts, S., Thoemel, J. and Munafo, A. "Radio communication blackout analysis of ExoMars re-entry mission using ray tracing method", AIAA 2021-0154, AIAA SciTech Forum 19–21 January 2021, VIRTUAL EVENT.

[19]Gabeaud, A., "Base Pressures at Supersonic Velocities". *Journal of Aeronautical Sciences (Readers'Forum)*, Vol. 17, No. 8, 1950, p. 525-526.

[20]Johnson, C.B., Bushnell, D. M, "Power-Law Velocity-Profile-Exponent Variations with Reynolds Number, Wall Cooling and Mach Number in a Turbulent Boundary Layer", NASA Technical Note D-5752, 1970.

[21]Khuri, A.I. and Cornell, J.A., *Response Surfaces: Designs and Analyses*, Statistics: textbooks and monographs Vol. 81, Marcel Dekker, Inc., New York, 1987.

[22]Box, G.E.P. and Wilson, K.B., "On the Experimental Attainment of Optimum Conditions", *Journal of the Royal Statistical Society*, Vol. B13, 1951, pp.1-38.

[23]Phadke, M.S., *Quality Engineering Using Robust Design*, Prentice-Hall, 1989.